Deterministic and probabilistic analysis of great-depth braced excavations: A 32 m excavation case study in Paris

Tingting Zhang, Julien Baroth, Daniel Dias, Khadija Nejjar

Journal Pre-proof

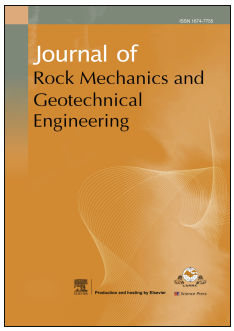

Deterministic and probabilistic analysis of great-depth braced excavations: A 32 m excavation case study in Paris

Tingting Zhang, Julien Baroth, Daniel Dias, Khadija Nejjar

PII: S1674-7755(24)00067-2

DOI: https://doi.org/10.1016/j.jrmge.2023.12.006

Reference: JRMGE 1423

To appear in: *Journal of Rock Mechanics and Geotechnical Engineering*

Received Date: 22 March 2023

Revised Date: 6 October 2023

Accepted Date: 28 December 2023

Please cite this article as: Zhang T, Baroth J, Dias D, Nejjar K, Deterministic and probabilistic analysis of great-depth braced excavations: A 32 m excavation case study in Paris, *Journal of Rock Mechanics and Geotechnical Engineering* (2024), doi: https://doi.org/10.1016/j.jrmge.2023.12.006.

Deterministic and probabilistic analysis of great-depth braced excavations: A 32 m excavation case study in Paris

Tingting Zhang [a], Julien Baroth [a], Daniel Dias [a,b,c,*], Khadija Nejjar [d]

[a] Université Grenoble Alpes, CNRS, Grenoble INP, 3SR, Grenoble, 38000, France
[b] Antea Group, Antony, 92160, France
[c] School of Automotive and Transportation Engineering, Hefei University of Technology, Hefei, 23009, China
[d] Terrasol, 42-52 Quai de la Rapée, Paris, 75012, France
*Corresponding author. E-mail address: daniel.dias@univ-grenoble-alpes.fr

Abstract: The Fort d'Issy-Vanves-Clamart (FIVC) braced excavation in France is analyzed to provide insights into the geotechnical serviceability assessment of excavations at great depth within deterministic and probabilistic frameworks. The FIVC excavation is excavated at 32 m below the ground surface in Parisian sedimentary basin and a plane-strain finite element analysis is implemented to examine the wall deflections and ground surface settlements. A stochastic finite element method based on the polynomial chaos Kriging metamodel (MSFEM) is then proposed for the probabilistic analyses. Comparisons with field measurements and former studies are carried out. Several academic cases are then conducted to investigate the great-depth excavation stability regarding the maximum horizontal wall deflection and maximum ground surface settlement. The results indicate that the proposed MSFEM is effective for probabilistic analyses and can provide useful insights for the excavation design and construction. A sensitivity analysis for seven considered random parameters is then implemented. The soil friction angle at the excavation bottom layer is the most significant one for design. The soil-wall interaction effects on the excavation stability are also given.
Keywords: Braced deep excavation; Soil-wall interaction; Stochastic finite element method; Horizontal wall deflection; Settlement; Failure probability

1. Introduction

Underground constructions have been developed rapidly in recent years to alleviate traffic congestion and ground surface land scarcity induced by urbanization and population growth. Excavations play a vital role in underground construction as they are necessary to create metro stations, ventilation systems or emergency exits. However, construction activities may induce excessive wall deflections or ground surface settlements, which may damage adjacent infrastructures and people's lives. The monitoring and an accurate estimation of the excavation performance at the serviceability limit state (SLS) are thus critical. Several relevant studies were conducted (Wang et al., 2005; Kung et al., 2007a; Baroth and Malecot, 2010; Ng et al., 2012; Tan and Wei, 2012; Hong et al., 2015; Zhang et al., 2015a, 2018a, b, 2019, 2021; Rouainia et al., 2017; Zheng et al., 2018; Zhao et al., 2022). However, these studies mainly focus on small-depth excavations from 6 m to 20 m, whereas studies on excavations at large depths (greater than 30 m) are rarely discussed.

This study discusses the serviceability and stability of great-depth excavations based on the Fort d'Issy-Vanves-Clamart excavation (FIVC) of the Grand Paris Express project. The FIVC excavation is located at southwest of Paris and is the first metro station of subway line 15. The excavation reaches a depth of 32 m, and Fig. 1 shows its location and aerial photo. It is seen that the FIVC metro station is surrounded by buildings and rail traffic systems. Therefore, it is important to control the construction activities influences.

(a)

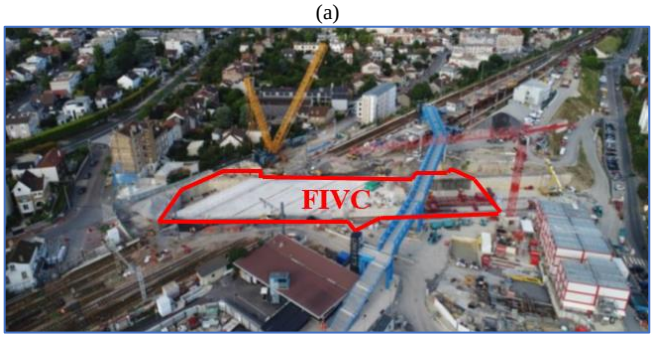

(b)

Fig. 1. Location (a) and aerial photo (b) of the FIVC excavation.

Empirical, analytical and numerical methods are commonly used for excavation stability analyses (O'Rourke, 1993; Zhang et al., 2015a; Yang et al., 2022). It should be noted that the empirical and analytical methods are mainly used for simple cases, such as hypothetical design examples with homogeneous soils. For problems with complex geological or geometrical conditions, numerical simulations will provide more accurate results since they can capture the effects of wall stiffness, complex soil behaviors, struts and soil-wall interactions on the excavation responses (Sert et al., 2016). Among numerical simulation methods, the finite element method (FEM) is one of the most popular methods used in the literature. It will be implemented in this study.

Besides, it is noted that soil randomness, which cannot be fully detected by a limited and cost-effective field investigation, exists due to the complex

formation process of the geological layers (Guo et al. 2018; Xue et al., 2023). The probabilistic analyses, which can consider parameter uncertainties, are more interesting and can provide more complementary results compared to the deterministic ones (Luo et al., 2012; Hamrouni et al., 2018). The failure probability can be determined by assessing the probabilities of maximum wall deflection (δ_{hm}) and maximum ground surface settlement (δ_{vm}) exceeding specified limiting criteria.

The Monte-Carlo simulation (MCS) was widely used for probabilistic analyses of excavations (Baroth and Malecot, 2010; Luo et al., 2018a, b; Nguyen and Likitlersuang, 2021; Zhang et al., 2023). However, the computational burden is strong if deterministic simulations are time-consuming or failure probabilities are small, which requires thousands of simulations to achieve a probabilistic analysis (Tran et al., 2021). In addition, different soil layers and corresponding soil parameters are involved in excavation stability analyses when dealing with a real case. There will be several random variables to be considered and a sensitivity analysis is necessary to determine the contributions of each parameter to the excavation responses. The global sensitivity analysis (GSA), which can consider the entire space of all concerned variables, is popular among the sensitivity analysis methods (Zhang et al., 2021). Whereas this analysis is related to the number of considered random variables and more simulations are required as the number of variables increases.

To address the limitations described above, this paper introduces a stochastic FEM based on the polynomial chaos Kriging (PCK) metamodel (MSFEM). This method can decrease greatly the computational effort with good accuracy by the fact that once the PCK surrogate model is constructed, the probabilistic analysis methods (i.e. MCS and GSA) can be implemented without further numerical simulations. Several probabilistic analysis results can then be provided including the failure probability (P_f), probability density function (*PDF*), cumulative distribution function (*CDF*), statistical moments of the system response and sensitivity indices of the considered random variables.

In this study, the stability of a great-depth FIVC excavation (32 m) of the Grand Paris project in France is discussed in deterministic and probabilistic frameworks. Finite element models are carried out to predict the wall deflection and surface settlement. The PCK metamodel-based stochastic FEM is proposed to improve considerably the probabilistic calculation efficiency. After the deterministic and probabilistic analysis results comparison, a series of studies is implemented to discuss the: (1) probabilistic distributions of the wall deflection and ground surface settlement, (2) relation between δ_{hm} and δ_{vm}, (3) probabilistic serviceability assessment with different limiting criteria, (4) sensitivity analysis for the considered parameters, and (5) soil-wall interaction effects on the excavation stability.

2. Project overview

The Fort d'Issy-Vanves-Clamart excavation, located in the suburbs of Paris, is the study case adopted. The FIVC excavation is about 110 m long, 22 m wide and 32 m deep. A cross-section of this excavation can be found in Fig. 2. It is located in the Parisian sedimentary basin and there are five strata below 77 m from the ground surface. It mainly consists of an 11 m-thick layer of backfill (BF), a 10 m-thick layer of hard limestone (HL), an 8 m-thick layer of Ypresian plastic clay (PC), a 10 m-thick layer of Meudon marls (MM) and the wall bottom is embedded into chalk (CK) (Nejjar et al., 2021).

To prevent damage to adjacent buildings and to the existing transportation system, this excavation is supported by a 40 m deep and 1.2 m thick diaphragm wall, a cover slab, floor levels (N1, N2, N3), strut level B4 and a raft. The retaining wall is embedded into MM and CK layers and the embedment depth *D* is 8 m. A top-down construction method is adopted and Table 1 summarizes the construction sequences. Seven parts are mainly divided for the excavation activities. The cover slab, floor levels N1, N2, N3, strut B4 and raft will then be installed respectively at stages I, III, V, VI and VII. The detailed excavation process and strut locations can be found in Fig. 2 and Table 1.

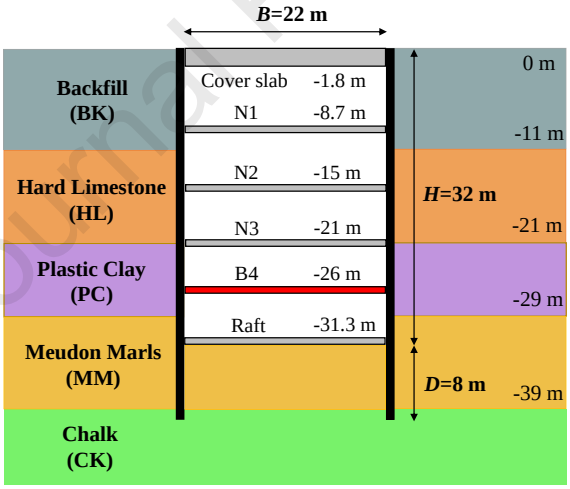

Fig. 2. FIVC section layout.

Table 1. Excavation stages.

Stage	Construction activity
I	Excavation to -10 m and install the cover slab and N1
II	Excavation to -14 m
III	Excavation to -16 m and installation of N2
IV	Excavation to -20 m
V	Excavation to -23 m and installation of N3
VI	Excavation to -27 m and installation of B4
VII	Excavation to -32 m and installation of raft

3. Metamodel-based stochastic FEM

This section aims to introduce the MSFEM. The deterministic finite element model and the involved probabilistic methods are presented first. It is followed by a detailed MSFEM analysis procedure.

3.1. Finite element modeling of the FIVC excavation

A two-dimensional (2D) finite element software, PLAXIS 2D, is adopted to analyze the excavation stability. One-half of the cross-section is modeled due to symmetry and the plane-strain numerical model is presented in Fig. 3. The horizontal and vertical lengths are respectively set equal to 100 m and 80 m to minimize the geometry influence. Displacements are fixed at the model bottom in horizontal and vertical directions, while only the horizontal direction is constrained for the lateral sides. A homogenized load of -30 kN/m/m is applied uniformly on the ground surface to consider the existing rail

traffic system and several buildings' effects. The total number of elements and nodes of the numerical model are respectively equal to 3448 and 28,178.

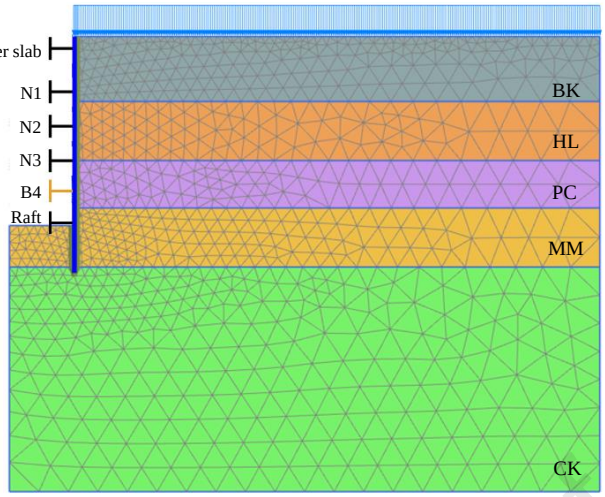

Fig. 3. FEM model of the FIVC excavation.

The hardening soil model (HS), which is an elastoplastic model and able to simulate the soil non-linearity and failure using the Mohr-Coulomb failure criterion, is used to simulate the soil behavior during the excavation phases. Table 2 summarizes the detailed soil parameters based on field tests (pressuremeter, cross hole and cone penetration tests), laboratory tests (oedometric and triaxial tests) and the numerical back analyses presented by Nejjar et al. (2021). It should be noted that the Ypresian plastic clay is over-consolidated by the fact that it was loaded with more than 120 m of sedimentary soils after the Ypresian age. Therefore, its initial earth pressure coefficient at rest k_0 is affected by both the friction angle and the over-consolidation ratio (OCR). The wall installation also influences the soil stress and the k_0 value is set equal to 0.85 (Mayne and Kulhawy, 1982; Nejjar et al., 2021).

Table 2. Soil parameters of each layer (Nejjar, 2019).

Parameter	Notation (unit)	Value				
		BK	HL	PC	MM	CK
Material model		HS	HS	HS	HS	HS
Unsaturated unit weight	γ_{dry} (kN/m^3)	19	21	19	19.5	19.5
Saturated unit weight	γ_{sat} (kN/m^3)	20	22	20	20.5	20.5
Secant stiffness	E_{50}^{ref} (MN/m^2)	48	200	150	600	1360
Tangent oedometer stiffness	E_{oed}^{ref} (MN/m^2)	48	200	150	600	1360
Unloading/reloading stiffness	E_{ur}^{ref} (MN/m^2)	144	600	450	1800	4080
Cohesion	c (kPa)	0	20	20	30	40
Friction angle	φ (°)	29	35	18	25	35
Poisson's ratio	υ_{ur}	0.2	0.2	0.2	0.2	0.2
Over-consolidation ratio	OCR	1	1	2.2	1	1
Initial earth pressure coefficient at rest	k_0	0.52	0.43	0.85	0.58	0.43

Vertical diaphragm walls were installed with a cover slab, floor levels N1, N2, N3, strut B4 and raft to ensure the excavation stability. The supports are modeled by fixed-end anchors considering a linear-elastic constitutive model and the corresponding parameters are presented in Table 3. Quasi-permanent loads are considered and applied on the cover slab, floor levels N1, N2, N3 and raft.

Table 3. Properties of the structural support elements (Nejjar, 2019).

Parameter	Notation (unit)	Value						
		Wall	Cover slab	N1	N2	N3	B4	Raft
Normal stiffness	EA (kN)	2.9×10^7	3.2×10^7	2.2×10^7	1.8×10^6	5.5×10^6	2.8×10^6	2.3×10^7
Flexural stiffness	EI (kN·m^2)	3.5×10^6						
Loading	F_y (kN)		-1370	-361	-59	-381		-70

3.2. Probabilistic analysis methods

The proposed MSFEM includes the construction of a metamodel polynomial chaos Kriging (PCK), the performance of the MCS and GSA.

3.2.1. Polynomial chaos Kriging

A polynomial chaos Kriging can be defined as a universal Kriging model that replaces the constant trend within an ordinary Kriging with a sparse set of orthogonal polynomials (Schöbi et al., 2017, Man et al. 2023). The basic formula is

$$Y \approx M^{\mathrm{PCK}}(\boldsymbol{X}) = \sum_{i\in A} \alpha_i \Phi_i(\boldsymbol{X}) + \sigma^2 Z(\boldsymbol{X}) \quad (1)$$

where $M^{\mathrm{PCK}}(\boldsymbol{X})$ is the PCK metamodel output, and $\boldsymbol{X}$ is a vector with the considered input random variables. The PCK trend $\sum_{i\in A} \alpha_i \Phi_i(\boldsymbol{X})$ is truncated to a finite number of terms for the sake of practical applications by using the hyperbolic truncation scheme. Its construction includes the determination of multivariate polynomial basis $\Phi_i(\boldsymbol{X})$, which is the tensor product of univariate orthonormal polynomials, and the corresponding unknown coefficients α_i, which are estimated by the Least-square minimization method (Pan et al., 2020). It is noted that a degree-adaptive method is carried out to determine the PCE order, which is set in the range of [1, 10] (Marelli and Sudret, 2014). A is the index set of polynomials. σ^2 and $Z(\boldsymbol{X})$ denotes respectively the variance and zero mean, unit variance stationary Gaussian process defined by an autocorrelation function $R(|x-x'|;\theta)$ between two sample points x and x', where the hyper-parameter θ needs to be estimated. The Matern-5/2 autocorrelation function is arbitrarily considered in this study.

PCK metamodel combines the advantages of the well-established PCE and Kriging techniques and aims to improve calculation efficiency and accuracy. More details about the PCK can be found in Schöbi et al. (2017).

3.2.2. MCS

MCS offers a simple way to estimate the random model response statistics (Bungenstab and Bicalho, 2016). It is widely used due to its simplicity and robustness, and is often used to evaluate the accuracy of other probabilistic methods. The idea is to generate samples crudely and evaluate the deterministic model response of each sample. For an MCS with N_{MCS} model evaluations, the failure probability can be determined by

$$P_{\mathrm{f}} = \frac{1}{N_{\mathrm{MCS}}} \sum_{k=1}^{N_{\mathrm{MCS}}} I_k \tag{2}$$

where the indicator function I_k is respectively set to 1 and 0 when samples belong to the failure and safe domains (i.e. $Y < 0$ and $Y \geqslant 0$, respectively). The limit-state function is detailed in Section 4.2. The accuracy of the results can be assessed by the coefficient of variation ($COV_{P_{\mathrm{f}}}$) of P_{f}, which is determined by

$$COV_{P_{\mathrm{f}}} = \sqrt{\frac{1-P_{\mathrm{f}}}{N_{\mathrm{MCS}} P_{\mathrm{f}}}} \tag{3}$$

The calculated results are more accurate with the N_{MCS} increase, whereas the computational effort increases at the same time. The target $COV_{P_{\mathrm{f}}}$ value is considered as 5% to balance the accuracy of the results and computational burden (Zhang et al., 2021).

3.2.3. GSA

GSA aims to quantify the effects of the input variables on the model response variability with consideration of the entire space of all concerned variables (Guo and Dias, 2020; Zhang et al., 2022). The Sobol-based GSA, which is based on the variance decomposition of the model output, is implemented in this study.

The first order Sobol' sensitivity index of a given variable x_i ($i = 1, ..., n$) can be determined by dividing the related partial variance V_i to the total variance V_{t}, which is expressed by

$$S_{Fi} = \frac{V_i(Y)}{V_t} = \frac{\mathrm{Var}[E(Y \| x_i)]}{V_t} \tag{4}$$

where $E(Y \| x_i)$ is the mean value of Y with consideration of all possible x values except x_i, and $\mathrm{Var}[E(Y \| x_i)]$ denotes the variance of $E(Y \| x_i)$ considering all possible values of x_i.

The corresponding total effect Sobol' index S_{Ti} for a variable x_i, which considers the interaction effects of the variable x_i with other variables, can be obtained by

$$S_{Ti} = S_{Fi} + \sum_{i \neq j} S_{ij} + ... + S_{1,...n} \tag{5}$$

3.3. Proposed MSFEM procedure

This study proposes the PCK MSFEM and this section aims to present the detailed procedure. To improve the efficiency and facilitate the automatic calculations, PYTHON and MATLAB languages were used for the pre- and post-processing of the probabilistic analyses. A flowchart of MSFEM is depicted in Fig. 4 and the details are described below:

(1) Preparation: determine the geometrical and geotechnical parameters and construct the FEM model as shown in Section 3.1. Determine the input parameters statistics (i.e. the distribution, mean value and coefficient of variation) and use MATLAB to generate an initial experimental design (ED) based on the Latin hypercube sampling (LHS). The ED initial size corresponds to the max[10, 2*N*], where *N* is the number of the considered random variables.

(2) Input-output sets determination: compile the batch commands and map the generated samples on the FEM model. The calculated results (i.e. the wall deflection and ground surface settlement) are then exported and saved automatically.

(3) Metamodel determination: construct an initial PCK metamodel based on the initial input-output sets and check the PCK metamodel accuracy. Two criteria, which correlate to the leave-one-out error (*LOO*) Err_{LOO} and failure probability convergence error $Err_{P_{\mathrm{f}}}$, are considered for the metamodel accuracy improvement:

$$\left.\begin{aligned} Err_{LOO} &= \frac{1}{N}\left[\frac{\sum_{i=1}^{N}(Y^{(i)} - \mu_{Y,(-i)}(x^{(i)}))^2}{\sigma^2_{Y,(-i)}(x^{(i)})}\right] \leq Err_{LOO\_\mathrm{tg}} \\ Err_{P_{\mathrm{f}}}(i) &= \max\left\{\left|\frac{P_{\mathrm{f}}(i) - P_{\mathrm{f}}(i-1)}{P_{\mathrm{f}}(i-1)}\right|, i \in [N_{\mathrm{en}} - N_{\mathrm{tg}} + 1, N_{\mathrm{en}}]\right\} \leq Err_{P_{\mathrm{f}}\_\mathrm{tg}} \end{aligned}\right\} \tag{6}$$

where $Y^{(i)}$ is the results from the FEM model, $\mu_{Y,(-i)}(x^{(i)})$ is the predictions from PCK metamodel using all the ED points except $x^{(i)}$, $\sigma^2_{Y,(-i)}(x^{(i)})$ is the estimated variance, $P_{\mathrm{f}}(i-1)$ and $P_{\mathrm{f}}(i)$ are respectively the (i–1)th and ith failure probabilities, N_{en} is the enrichment samples number, N_{tg} is the number of failure probability needs to be compared, and Err_{LOO_tg} and $Err_{P_{\mathrm{f}}\_\mathrm{tg}}$ are the threshold values for both criteria. Err_{LOO_tg}, $Err_{P_{\mathrm{f}}\_\mathrm{tg}}$ and N_{tg} are respectively set to 0.01, 0.01 and 10 in this study (Pan and Dias, 2017). Once the Err_{LOO} and $Err_{P_{\mathrm{f}}}$ are smaller than the values of Err_{LOO_tg} and $Err_{P_{\mathrm{f}}\_\mathrm{tg}}$, the procedure enters the next step. Otherwise, ED enrichment for the PCK metamodel construction is necessary. The *U*-function is performed in this study, which is expressed by

$$U(x) = \frac{|\mu(x)|}{\sigma(x)} \tag{7}$$

The newly added sample is chosen by minimizing Eq. (7), i.e. $S_n = \arg\min U(x)$, which permits finding the point which has the highest probability of being misjudged as failure or safety. The optimal candidates can then be placed into the existing ED and a metamodel can be constructed based on the improved ED.

(4) Probabilistic analysis: perform the probabilistic analysis methods based on the PCK metamodel and export results, which include (I) MCS: failure probability, model response distributions and statistical moments of the system response (mean value and standard deviation); (II) GSA: first-order sensitivity index and total effect sensitivity index. It should be noted that not only the mentioned probabilistic analysis methods but also others, such as the first order reliability method and the subset simulation, can be performed after the PCK construction.

The input-output sets preparation is achieved by PLAXIS 2D V20, the input parameters import and results export are implemented by PYTHON 3.8 and MATLAB 2016, and the PCK-based probabilistic analysis is written in MATLAB. The mentioned calculations are performed on a computer with an Intel (R) Core (TM) i7-8700K 3.70GHz CPU.

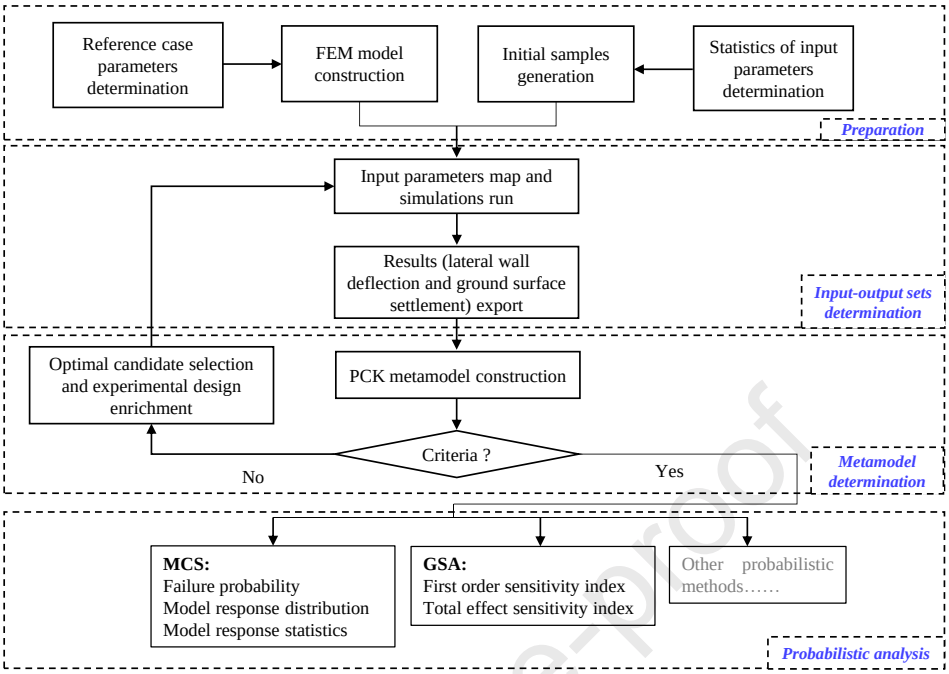

Fig. 4. Flowchart of the proposed MSFEM.

4. Results and comparison

The deterministic numerical simulation for the FIVC excavation is first validated by comparison with field measurements, empirical methods and case histories. The performance of the proposed MSFEM is then discussed.

4.1. Deterministic analysis

4.1.1. Field measurements

A comprehensive monitoring system (such as wall inclinometers and optical fiber) was implemented to assess the excavation performance (Nejjar, 2019). Fig. 5a depicts the measured and simulated excavation-induced wall deflection profiles at Stages IV, V and VI. It is seen that the trend and magnitude of the simulated horizontal wall deflections are generally in good agreement with the measured ones. It allows to validate the numerical model effectiveness. Besides, the maximum horizontal wall deflection is increased by about 6 mm from stage IV to stage V, which is larger than the increment from stage V to stage VI (2 mm). This is because the horizontal wall deflection is strongly related to the soil behavior behind the retaining wall. The soil stiffness difference between layers HL, PC and MM causes the wall to deflect more easily at layer PC. N3 floor was installed at the stage V and it is located at the junction between layers HL and PC. Conversely, at stage VI, strut B4 is installed in the layer PC middle, which can resist effectively the wall deformation. In addition, no toe movements occurred since the diaphragm wall is embedded into the layers MM and CK with high stiffness. It is worth noting that the measured displacements start at the 7 m deep excavation level, as the diaphragm wall is cast at this level and then extends upwards to the backfill and ground level (Nejjar, 2019; Nejjar et al., 2021).

Fig. 5b presents a comparison of the observed and computed ground surface settlements at Stages IV and VI. The ground surface settlement trends are similar, while the FEM simulation overestimates the settlement magnitudes. The possible explanation is that the railway tracks above the excavation were still in operation during the FIVC station construction and the loads applied on the ground surface may vary in time. In this numerical model, a static uniform load of -30 kN/m^2 is assumed to be distributed on the ground surface for the sake of simplicity and the load variations are not considered. Besides, compared with the wall deflection measurements, the surface settlement data is relatively scattered and cannot totally be used to identify the surface settlement contours.

The deterministic FEM model implemented in this study is able to reflect reasonably the excavation phases and will be used in the following discussions.

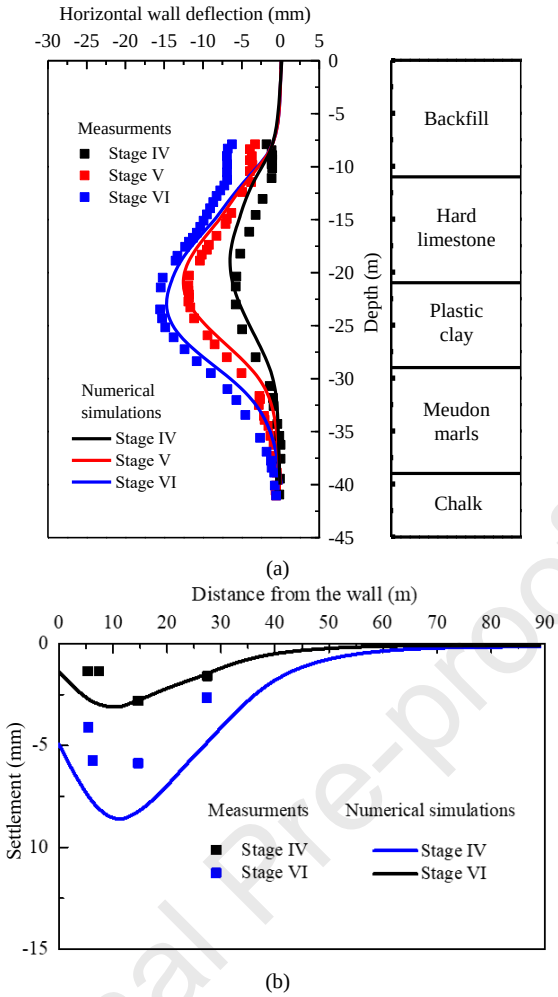

Fig. 5. Comparison between measured and predicted excavation responses: (a) Horizontal wall deflection, and (b) Ground surface settlement.

4.1.2. Empirical methods and case histories

Fig. 6a depicts the development of the maximum horizontal wall deflection δ_{hm} during construction. It can be observed that the ratio R_d, which denotes the relationship between δ_{hm} and the excavation depth H, ranges from 0.05‰ to 0.2‰ when H is smaller than 16 m. δ_{hm} varies almost linearly with the excavation depth when H lies between 23 m and 32 m, and the corresponding R_d value is close to 0.58‰. The R_d value increase lies in the fact that the plastic clay is involved in excavation activities with H being larger than 21 m, and the stiffness decrease of layer PC can increase the wall deflection.

Some existing empirical relationships are also provided for comparison. It can be seen that the wall deflection is significantly smaller than the reported ones, which include (0.2%-1%)H in soft clays (Peck, 1969), (0.22%-0.5%)H in stiff clays (Clough and O'Rourke, 1990) and (0.3%-0.6%)H in soft-medium clays (Kung et al., 2007a). Tan and Wei (2012) provided a R_d range of (0.2‰-0.23%)H in Shanghai soft clays and the lower bound 0.2‰H is relatively close to the present study one, whereas the excavation depth is limited to 18 m. One documented deep excavation (38 m) is also given, and the δ_{hm} value is around 0.14%H (Liu et al., 2011).

The relationship between the maximum ground surface settlement δ_{vm} and excavation depth H can be found in Fig. 6b. R_s is the ratio between δ_{vm} and H. It is seen that the results are consistent with the wall deflection ones, and the surface settlements of Stages I, II and III are very small with R_s (around 0.03‰). The magnitude of δ_{vm} increases with H within an upper bound of R_d = 0.45‰. The settlement values in this study are also smaller than those of the documented excavations: (0.15%-0.5%)H in stiff clay (Clough and O'Rourke, 1990), (0.3‰-0.18%)H of Shanghai soft clay (Tan and Wei, 2012) and 0.45‰ for a 38 m deep excavation (Liu et al., 2011).

The small values of δ_{hm} and δ_{vm} can be explained by the fact that a considerable thickness of hard layers (HL, MM and CK) is present along the excavation and the diaphragm wall is also embedded into the layers MM and CK. It can effectively prevent excavation deformation. The installation of several supports, which include the diaphragm wall, cover slab, raft and struts, can also increase the excavation stability.

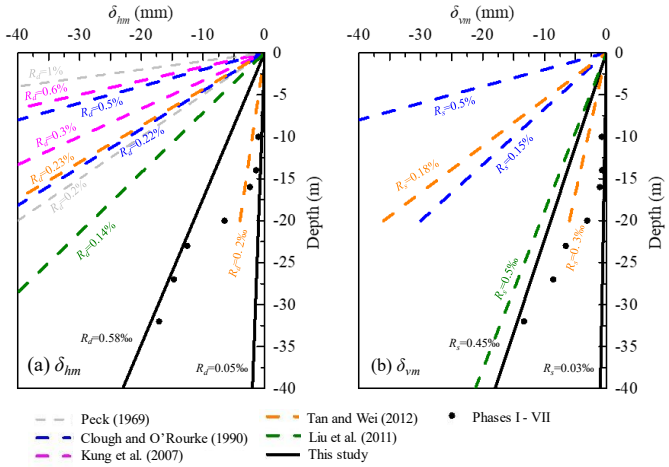

Fig. 6. Relationships of maximum horizontal wall deflection and maximum ground surface settlement with excavation depth.

Fig. 7 gives the locations where the maximum wall deflection and maximum ground surface settlement occur with the increase in excavation depth. There is no doubt that the location of δ_{hm} moves downward with the H increase. For stages I, II and III, δ_{hm} is approximately located 3 m above the excavation bottom. When H approaches 20 m, the location is close to the excavation bottom. For the rest of the excavation phases (stages V, VI and VII), the maximum wall deflection falls within the layer PC due to its relatively small stiffness contrast with the adjacent layers (HL and MM). The maximum surface settlement is located at 4-7 m from the retaining wall for stages I, II and III. The location changes slightly when H is larger than 20 m and is mainly distributed around 10 m from the wall. Construction at these locations should be particularly careful and strengthening measurements need to be implemented to prevent uneven settlements and potential damages.

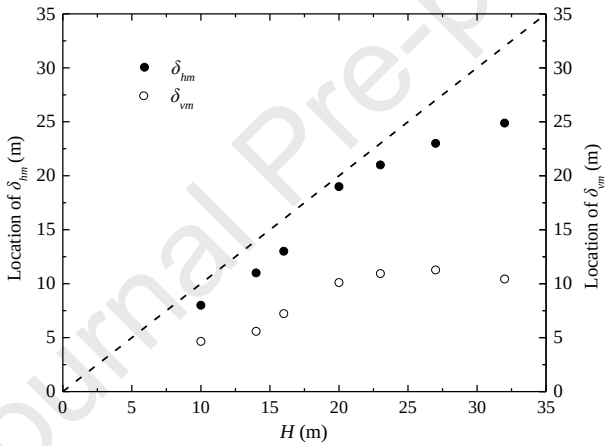

Fig. 7. Locations of maximum wall deflection and maximum ground surface settlement with increase in excavation depth.

4.2. Probabilistic analysis

4.2.1. Definition of the limit state function and statistical parameters

The excavation design and construction need to satisfy the horizontal wall deflection and ground surface settlement requirements at the serviceability limit state, i.e. the values of δ_{hm} and δ_{vm} should be smaller than the defined limiting values. In this study, the probabilistic analysis related to the wall deflection is considered (the explanations are detailed in Section 5.3) and the limit state function is defined by

$$g(\boldsymbol{X})=\delta_{hm}-\delta_{hm\_lim} \quad (8)$$

where $\boldsymbol{X}$ denotes the considered random variables, $g(\boldsymbol{X})$ is the limit state function regarding the maximum wall deflection, and δ_{hm_lim} is the limiting maximum wall deflection and is set equal to 28 mm in this study (Philipponnat and Hubert, 2016). The excavation is considered as safe when $g(\boldsymbol{X}) \leq 0$, and failure occurs when $g(\boldsymbol{X}) > 0$.

Parameter uncertainties of layers HL, PC and MM are considered since the excavation is done through these three layers. Seven random variables, which include the friction angle and secant stiffness of layers HL, PC and MM, and the initial earth pressure coefficient at rest of layer PC, are discussed (Nejjar, 2019). It was noted that due to cost issues, limited experiments were conducted to determine the soil properties, which cannot be used for the determination of the statistical information. Therefore, the statistical properties are determined by the existing studies (Guo et al., 2019; Phoon and Kulhawy, 1999) and are summarized in Table 4. The input uncertain parameters are considered as statistically independent and a lognormal distribution is taken into account to model the sample distribution. Besides, more cases with different *COV* values are discussed to provide more practical suggestions for similar excavations, which is presented in Section 5.

Table 4. Statistics of input random variables.

Layer	Parameter	Notation (unit)	Statistics of parameters	
			Mean	Coefficient of variation (*COV*)
HL	Friction angle	φ_{HL} (°)	35	0.1[a]
	Secant stiffness	$E50^{ref}_{HL}$ (kN/m^2)	2×10^5	0.15[a]
PC	Friction angle	φ_{PC} (°)	18	0.1
	Secant stiffness	$E50^{ref}_{PC}$ (kN/m^2)	1.5×10^5	0.15
	Initial earth pressure coefficient at rest	k_{0PC}	0.85	0.15[b]

MM	Friction angle	φ_{MM} (°)	25	0.1
	Secant stiffness	$E50^{ref}_{MM}$ (kN/m^2)	6×10^5	0.15

[a] Based on values given by Phoon et al. (1999).
[b] Guo et al. (2019).

4.2.2. Probabilistic results

The proposed PCK metamodel-based stochastic FEM presented in Section 3 is implemented. The PCK-based MCS provides a failure probability of 3.6×10^{-4}. In order to satisfy the COV_{P_f} requirement (5%) defined in Eq. (3), a total 1.11 million simulations are performed after a numerical convergence study. The corresponding maximum wall deflection distribution is depicted in Fig. 8. It is found that δ_{hm} is mainly distributed in the range of [12.5 mm, 25 mm], and there is a probability of 3.6‰ exceeding the limiting wall deflection value (28 mm). The statistical moments of the system response are respectively the mean value and standard deviation of 17.9 mm and 2.2 mm.

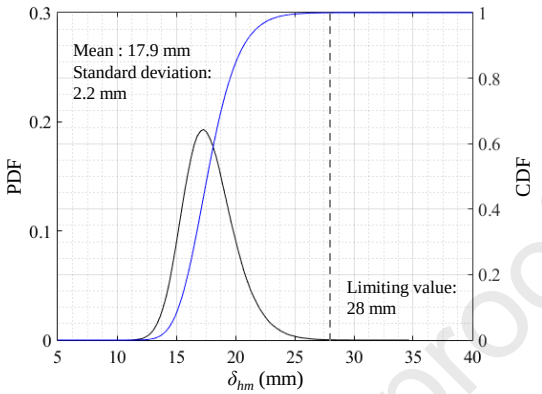

Fig. 8. PDF and CDF of maximum wall deflections of PCK-MCS.

Fig. 9 depicts the PCK-based GSA analysis results. Although there are small differences in the magnitudes of the first-order and total-effects Sobol indices, they can give a consistent ranking order. Besides, the friction angle plays a dominant role in the wall deflection variation within the current probabilistic input configuration, and one of layer MM contributes the most, followed by layers PC and HL. The possible explanation can be found in Fig. 10, which depicts 4 plastic zone distributions with different friction angles of layers MM and PC. The corresponding magnitudes are determined considering the mean ± three times the standard deviation.

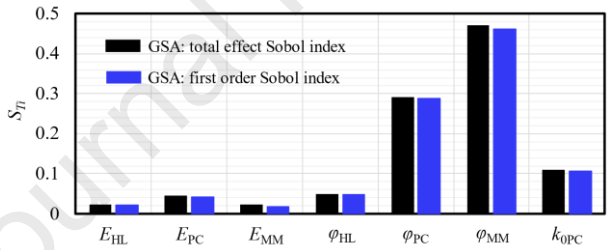

Fig. 9. Sensitivity analysis results of PCK-GSA.

It can be observed that when the friction angle of layer MM is large, the failure points are mainly distributed at the soil-wall interface, and the intersection of the wall and the excavation base is found to have a direction being around 45° as shown in Fig. 10a. However, when its friction angle value decreases, the failure points move to the retaining wall back and the failure surface is through layer MM. It even reaches the wall toe due to the reduced shear strength. Soil deformations in layer MM increase the active earth pressure on the wall and subsequently induce significant wall deflections due to the deformation compatibility. Besides, the connection of the shear failure surface and the wall toe may lead to wall toe deformation and greatly decreases the excavation stability.

Comparatively, the effects of the PC layer friction angle on the plastic zone distributions are presented in Fig. 10c and d. Similar results are achieved. The friction angle decrease can make the failure points move behind the wall. However, it can only affect the excavation phase's depth range, i.e. the upper MM layer part. Correspondingly, the friction angle influence on the horizontal wall deflection is small.

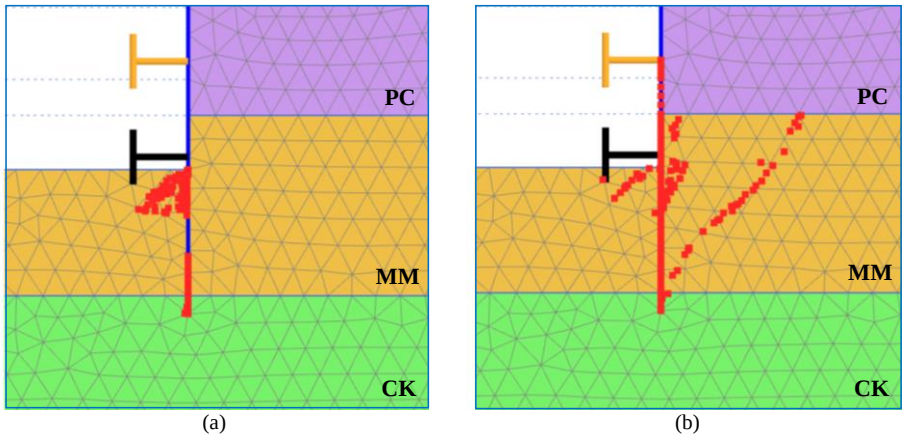

(a) (b)

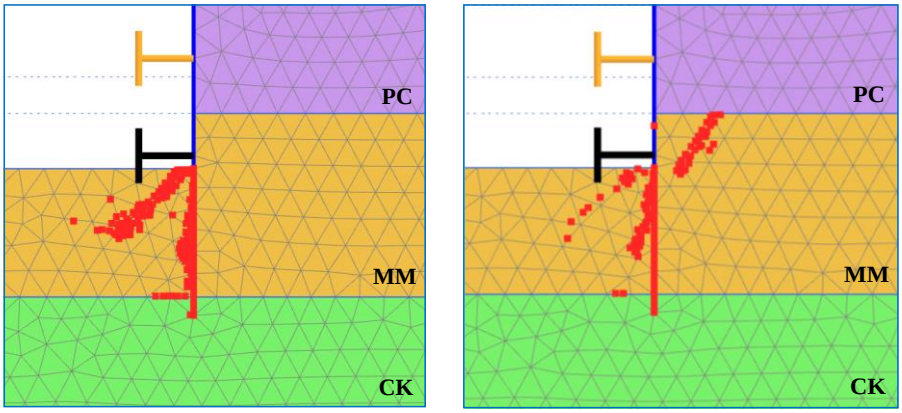

(c) (d)

Fig. 10. Influences of the friction angles of layers MM and PC on the plastic zone distributions: (a) φ_{MM} = 32.5°, φ_{PC} = 18°; (b) φ_{MM} = 17.5°, φ_{PC} = 18°; (c) φ_{MM} = 25°, φ_{PC} = 23.4°; and (d) φ_{MM} = 25°, φ_{PC} = 12.6°.

In addition, the bending moment and wall deflection profiles are also presented in Fig. 11 to provide a quantitative interpretation. It is seen that the MM friction angle decrease leads to the increase of the bending moment at layer MM (2114 kN m/m) and subsequently induces an increase of the horizontal wall deflection. The δ_{hm} value is up to 26 mm with an increase of 76.4% compared to the case of φ_{MM} = 32.5° (14.8 mm) and the maximum wall deflection location is lowered to the intersection of layers MM and PC. Conversely, the bending moment and wall deflection variations with the PC friction angle decrease are less significant. The maximum wall deflection difference is around 50.7% and occurs mainly in the middle of layer PC. In summary, the layer MM friction angle has an essential effect on the excavation stability and its value should be determined with caution during design and construction.

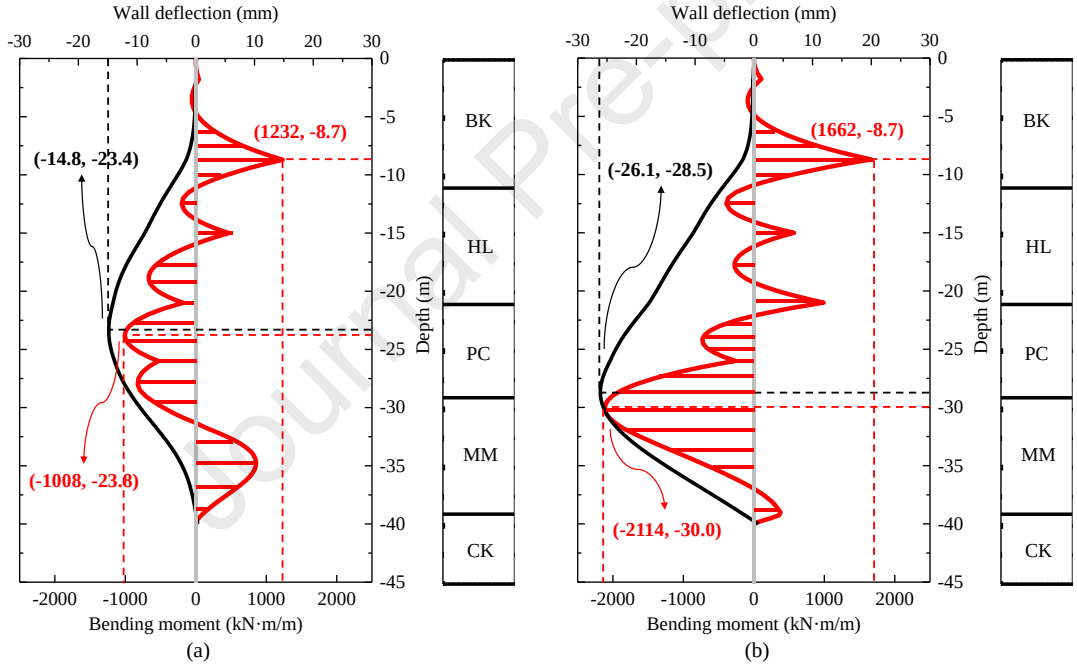

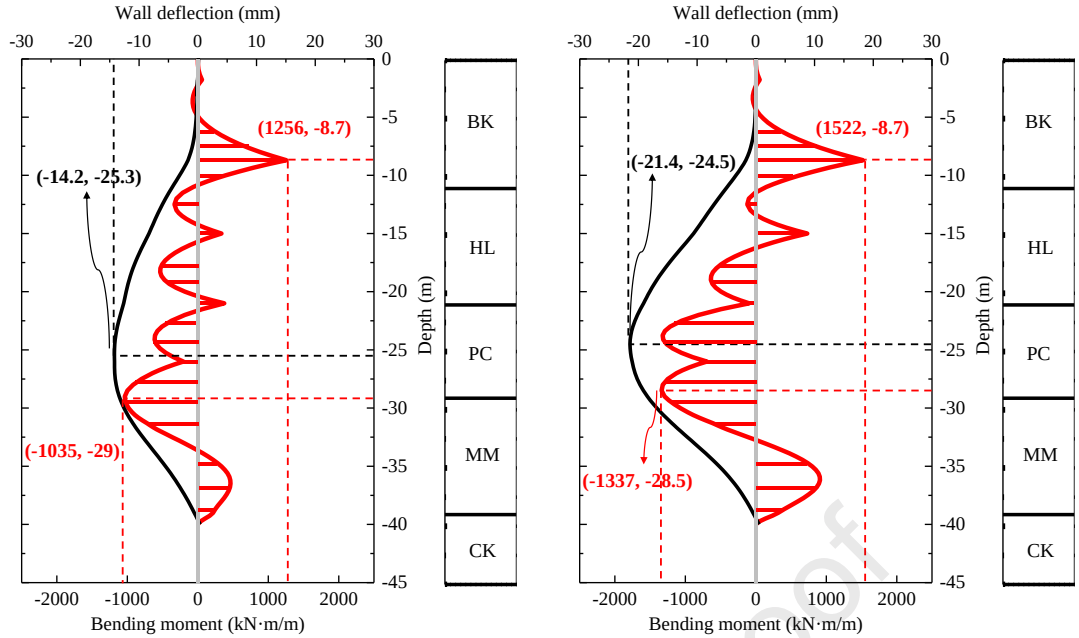

Fig. 11. Influences of MM and PC friction angles on the wall bending moment and horizontal deflection: (a) φ_{MM} = 32.5°, φ_{PC} = 18°; (b) φ_{MM} = 17.5°, φ_{PC} = 18°; (c) φ_{MM} = 25°, φ_{PC} = 23.4°; and (d) φ_{MM} = 25°, φ_{PC} = 12.6°.

The sensitivity index of the initial earth pressure coefficient at rest of layer PC follows with being around 0.1. Its importance can be explained by the stiffness difference between the PC and adjacent layers (HL and MM), which may lead to the maximum wall deflection more likely to occur at layer PC as presented in Fig. 7. The k_{0PC} affects the lateral stress magnitudes, and the wall deflection will be directly affected. For the secant stiffness, layer PC contributes the most among the considered layers. It can also be explained by the fact that the maximum wall deflection is more prone to occur in layer PC and the corresponding stiffness is more sensitive to the wall deflection.

4.2.3. Accuracy and efficiency survey

Fig. 12 depicts the numerical convergence of the leave-one-out error Err_{LOO} and of the failure probability error Err_{P_f}. The criterion for *LOO* is satisfied when 8 samples are added. P_f values vary considerably for the former 100 sample enrichments, and start to converge after 131 and Err_{P_f} satisfies the requirement after 141 sample enrichments. A total of 155 evaluations, including 14 initial EDs, are used for the PCK metamodel construction to satisfy the criteria presented in Eq. (6).

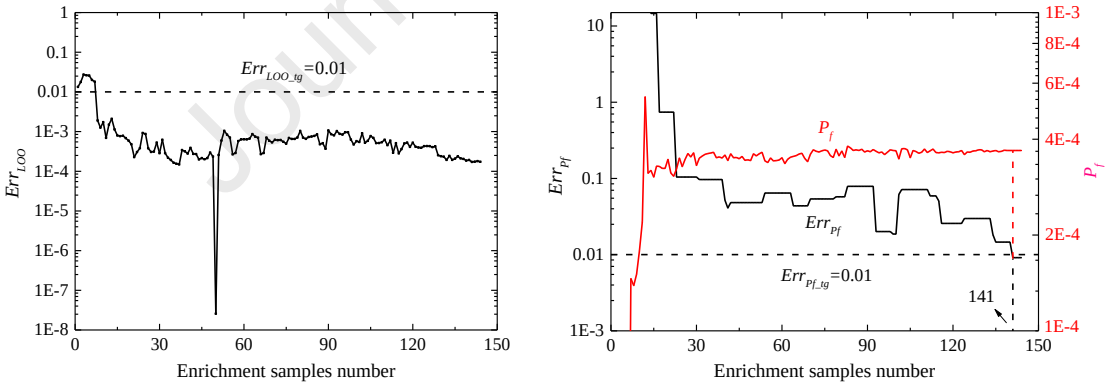

Fig. 12. PCK metamodel construction process with the enrichment samples increase: (a) Err_{LOO} and (b) Err_{P_f}.

The PCK metamodel accuracy should be validated by comparing the probabilistic results obtained by a direct MCS and a direct GSA. However, it should be noted that at least 1.11 million samples are necessary for the MCS calculation and further 9000 simulations for the GSA. It requires about 3886 d using the direct probabilistic methods, which is unaffordable in practice (one simulation needs around 300 s). Therefore, the proposed procedure accuracy is discussed by the metamodel performance. If the estimated wall deflection estimations based on the PCK metamodel are accurate enough, the subsequent probabilistic methods can perform in a good manner.

The metamodel performance can be found in Fig. 13. The maximum wall deflection values obtained from the PCK metamodel are validated by comparing with the 2D numerical evaluations. It is seen that the points are distributed on a line at 45° and the R^2 value can be up to 0.994, which means that the PCK metamodel can provide similar δ_{hm} as the numerical simulations. The effective PCK predictions can then ensure the accuracy of the following probabilistic discussions.

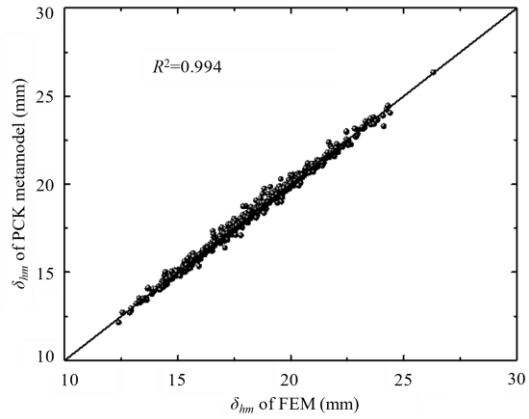

Fig. 13. Maximum horizontal wall deflection comparison using FEM and PCK methods.

Therefore, this proposed MSFEM can decrease significantly the number of numerical evaluations and make the probabilistic analysis affordable with accurate results. It will be used in the following probabilistic discussions.

5. Discussion

This section aims to investigate the (1) uncertainties consideration effects on the wall deflection and surface settlement distributions, (2) relationship between the maximum wall deflection and maximum surface settlement, (3) probabilistic serviceability assessment with different limiting values, and (4) soil-wall interaction effects on the excavation stability.

5.1. Probabilistic distributions of the wall deflection and ground surface settlement

Four cases with different combinations of *COV* for 7 random variables are considered and details are given in Table 5. Case A is the reference case, and the *COV* values of secant stiffness, friction angle and initial earth pressure coefficient at rest are respectively increased by 0.1 for cases B, C and D, while the other parameters are kept constant. Five hundred realizations (samples are generated using LHS) are simulated for each case to investigate the uncertainty effects on the wall deflections and ground surface settlements.

Table 5. Four cases for probabilistic analysis.

Case	COV_{E50ref}	COV_{φ}	COV_{k0}
A	0.15	0.1	0.15
B	0.25	0.1	0.15
C	0.15	0.2	0.15
D	0.15	0.1	0.25

The mean values of the maximum wall deflection and ground surface settlement are respectively given in Fig. 14a and b. The deterministic FEM analysis results are also presented for comparison. The mean values are larger than the deterministic ones, and the magnitude is increased with the uncertainty level. Therefore, the excavation stability will be overestimated when the uncertainty is neglected or the uncertainty level is underestimated. It is also observed that there is a significant increase in cases C and D compared to case A, while case B is relatively close to case A.

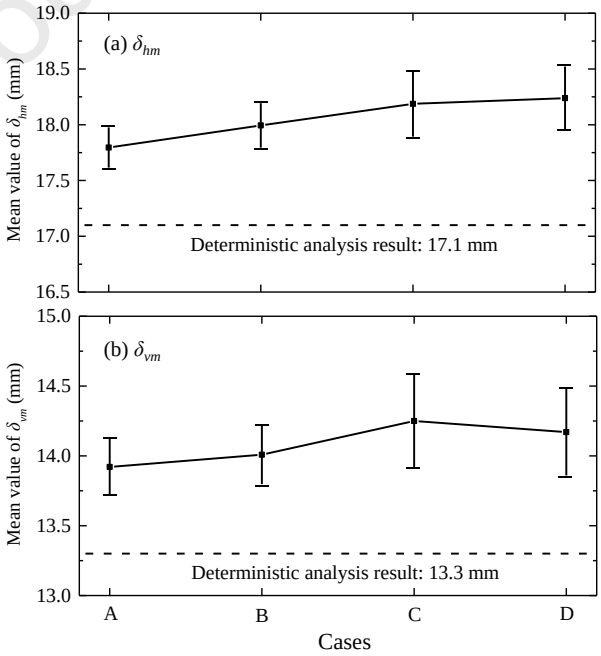

Fig. 14. Mean values of the maximum wall deflection and maximum ground surface settlement under different cases.

A confidence interval at 95% level for the mean values is also presented to discuss the parameter variability and the result accuracy. It is observed that the confidence bound width is affected by the input parameters' uncertainty level. Case A has the narrowest confidence interval due to the smallest *COV* combinations. The confidence intervals of case C are the largest. They are followed by cases D and B. It demonstrates that the friction angle *COV*

increase leads to more varied wall deflections and ground surface settlements whereas the secant stiffness is the least sensitive one. It is consistent with the sensitivity analysis results presented in Fig. 9. Besides, the confidence intervals for ground surface settlement are greater than the wall deflection ones, which is similar to the results of Nguyen and Likitlersuang (2021).

It is noted that the confidence interval is also affected by the number of considered simulations, i.e. a large number of simulations can reduce the interval and improve the analysis results accuracy. However, there is no significant improvement in the analysis results when the simulation number is greater than a certain value, whereas the computational efforts are increased. A simulation number sensitivity analysis is necessary to balance the accuracy and computational burden. Fig. 15 displays the numerical convergence of the estimates of mean values and standard deviation (Std.) for δ_{hm} and δ_{vm}. It can be observed that case A with small *COV* values is more prone to converge and there is no prominent change for cases B, C and D after 300 simulations. It confirms the accuracy and rationality of the results based on 500 simulations for each case in this study.

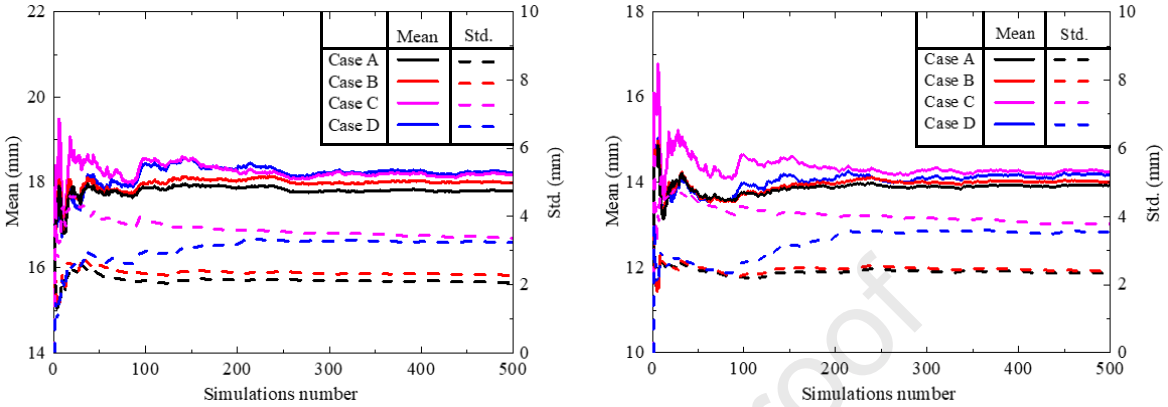

Fig. 15. Numerical convergence of mean values and standard deviation for the maximum wall horizontal deflection and surface settlement: (a) δ_{hm} and (b) δ_{vm}.

The distributions of the wall deflection and ground surface settlement are plotted respectively in Figs. 16 and 17. The deterministic analysis (DA) contour is also shown for comparison. It is seen that the wall deflection and ground surface settlement obtained by the deterministic analysis are included in the probabilistic analysis (PA) distribution range, while the probabilistic analysis gives further possible cases compared to the deterministic one. It allows for providing more references for the excavation design and construction. Besides, case A gives the narrowest wall deflection and ground surface settlement distribution and the ranges are greater as the *COV* value increases. Case C has the most significant variation, which is followed by cases D and B (taking the wall deflection as an example, the ranges are respectively [-13 mm, -26.5 m], [-10.4 mm, -28.6 m] and [-11 mm, -28.5 m] for cases B, C and D). It indicates again that the friction angle is more sensitive to the horizontal wall deflections and ground surface settlements compared with other parameters (secant stiffness and initial earth pressure coefficient at rest).

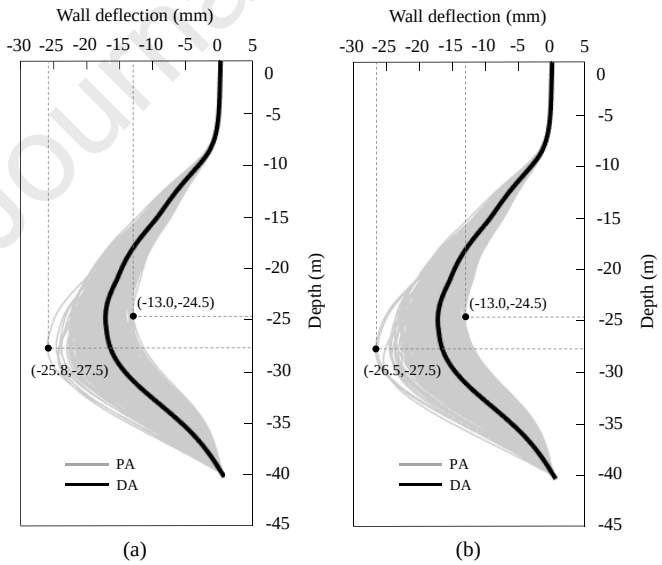

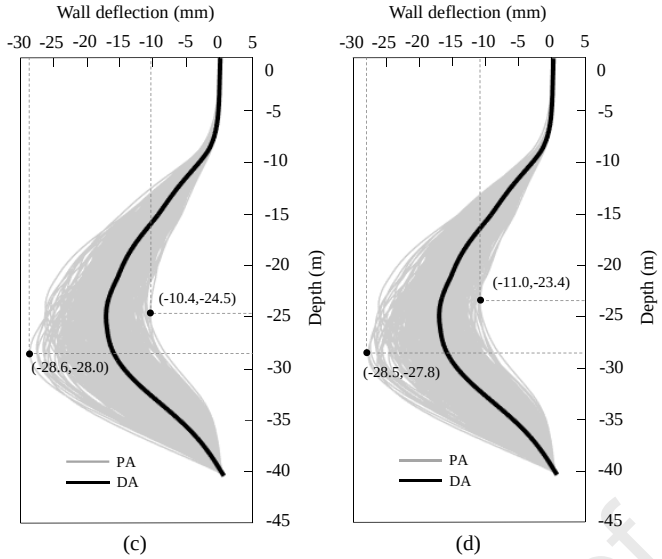

Fig. 16. Wall deflection contours using deterministic and probabilistic analyses: (a) Case A, (b) Case B, (c) Case C, and (d) Case D.

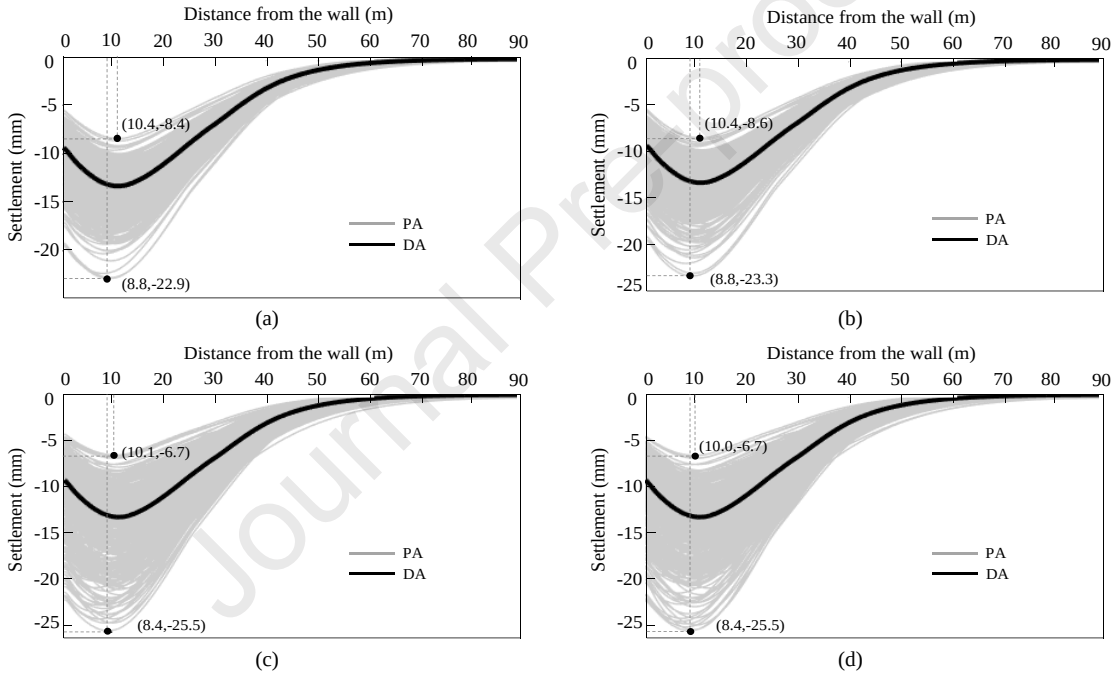

Fig. 17. Ground surface settlement contours using deterministic and probabilistic analyses: (a) Case A, (b) Case B, (c) Case C, and (d) Case D.

In order to specify the probability of overestimation and underestimation for the wall deflection and ground surface settlement, the PDF and CDF of δ_{hm} and δ_{vm} based on 500 realizations are presented in Fig. 18. For the maximum wall deflections, about 36%-42% of the probabilistic simulations are smaller than the deterministic one, while the percentage range is 42%-48% for the ground surface settlements. In addition, the overestimation probability of case C is the smallest. It is followed by cases D, A and B. It can be explained by Figs. 16 and 17 that the wall deflection and surface settlement distribution ranges are wider for case C and more cases with small magnitudes are generated.

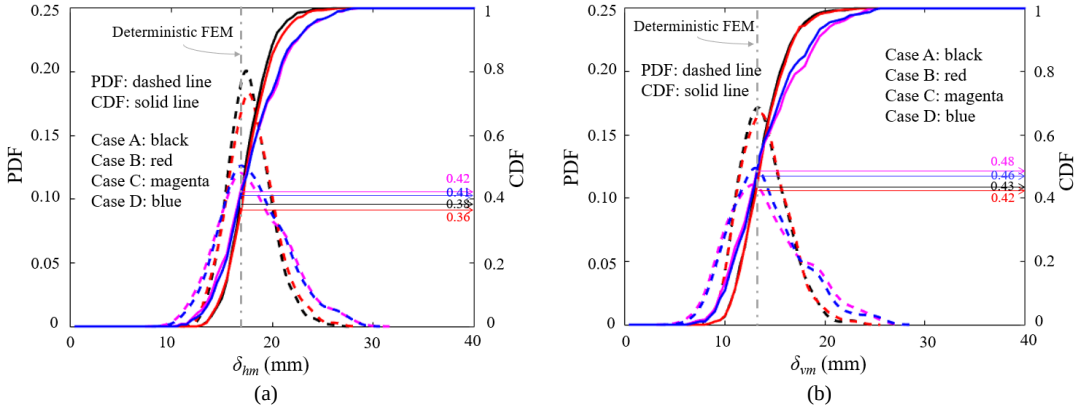

Fig. 18. PDF and CDF of maximum wall deflections and ground surface settlements: (a) δ_{hm} and (b) δ_{vm}.

The location determination where the maximum wall deflection and maximum ground surface settlement occur is important for the structural assessment of diaphragm walls and the construction of adjacent buildings. Fig. 19 depicts the depth frequency at which the maximum wall deflection occurs for different cases. It is observed that the δ_{hm} locations are distributed widely as the *COV* value increases ([22 m, 30 m] for cases A and B; [18 m, 30m] for cases C and D). However, the depths are mainly located between 24 m and 26 m below the ground surface (case A: 62%, case B: 59%, case C: 36% and case D: 41%) due to the stiffness difference between layers HL, PC and MM.

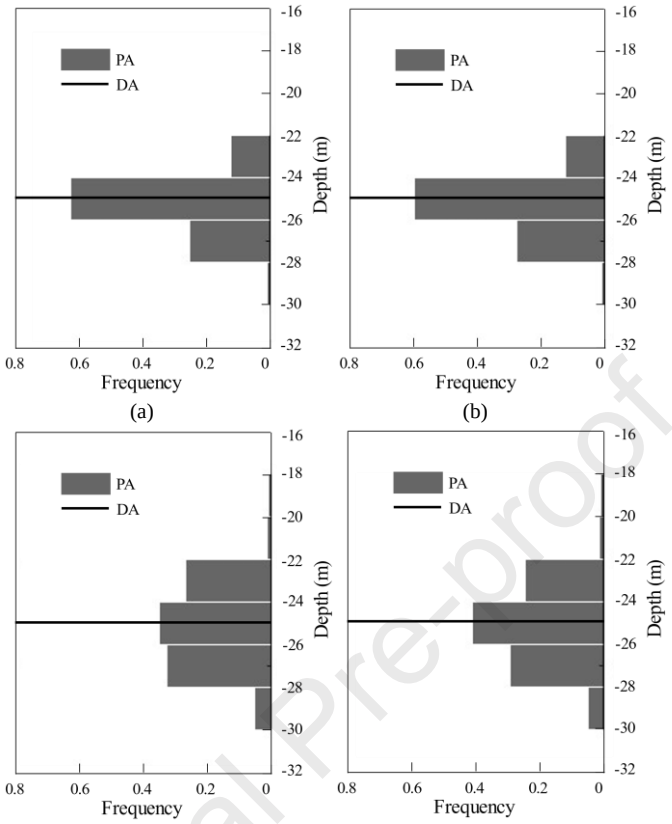

Fig. 19. Frequency of the maximum horizontal wall deflection location: (a) Case A, (b) Case B, (c) Case C, and (d) Case D.

Fig. 20 shows the distance from the diaphragm wall distributions where the maximum ground surface settlement occurs. The δ_{hm} is located between 6 m and 12 m from the diaphragm wall for cases A and B, and the range increases to [4 m, 14 m] for cases C and D, whereas the maximum surface settlements mainly occur in the range of 10 m to 12 m from the wall. Therefore, the construction activities should be considered and monitored in the influence zone of the ground surface settlement (80 m, approximately 2.5 times the excavation depth as shown in Fig. 17), particularly in the range of [10 m, 12 m], where most of the maximum surface settlements outcomes are observed.

In addition, similar results are achieved for the wall deflections and ground surface settlements and the deterministic results lie in the highest frequency range of the probabilistic analysis.

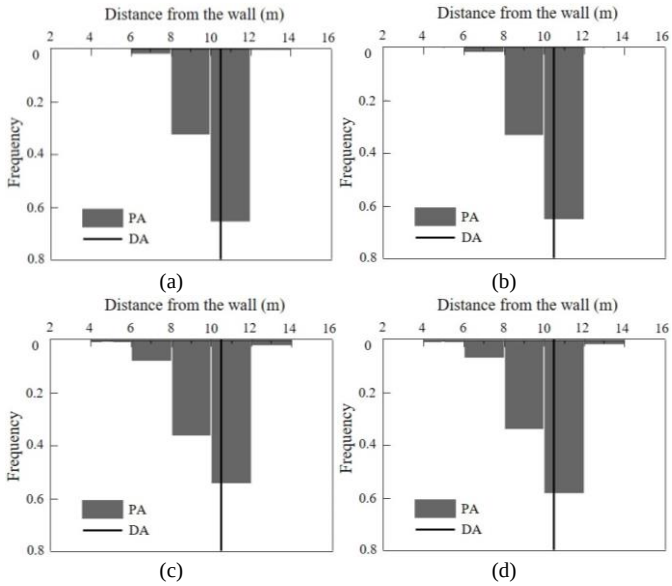

Fig. 20. Frequency of the maximum ground surface settlement location: (a) Case A, (b) Case B, (c) Case C, and (d) Case D.

5.2. Relation between the wall deflection and ground surface settlement

This section investigates the relation between the maximum wall deflection and maximum ground surface settlement under 4 cases presented in Table 5. Fig. 21 plots the δ_{hm} distributions versus the ratio between δ_{vm} and δ_{hm}. As expected, with the *COV* level increase, the points are more dispersed. However, the ratio δ_{vm}/δ_{hm} is generally within the range of [0.5, 1], which is similar to the existing studies (Kung et al., 2007b; Tan and Wei, 2012). It means that the maximum ground surface settlements are smaller than the maximum wall deflections and there is a positive linear relation between δ_{vm} and δ_{hm}. The ratio histogram distributions are presented in the upper part of each subfigure and it is observed that most of the ratios fall between 0.7 and 0.8 regardless of the uncertainty effect.

In addition, there is a trend between the ratio and the maximum wall deflections from the scatter figures. The ratio distributions within 4 deflection ranges ([10 mm, 15 mm), [15 mm, 20 mm), [20 mm, 25 mm), [25 mm, 30 mm]) are discussed and the results can be found in the right part of each subfigure. It can be observed that the ratio tends to be greater for cases with large δ_{hm} values. Taking case C as an example, when the δ_{hm} falls between 10 mm and 15 mm, the ratio varies from 0.5 to 0.9 and most of the cases are within the range of [0.7, 0.8]. However, the ratios are mainly located between 0.8 and 0.9 when the δ_{hm} is larger than 20 mm. Therefore, it is more rational and conservative to consider larger δ_{vm}/δ_{hm} ratios for cases with larger values of δ_{hm}.

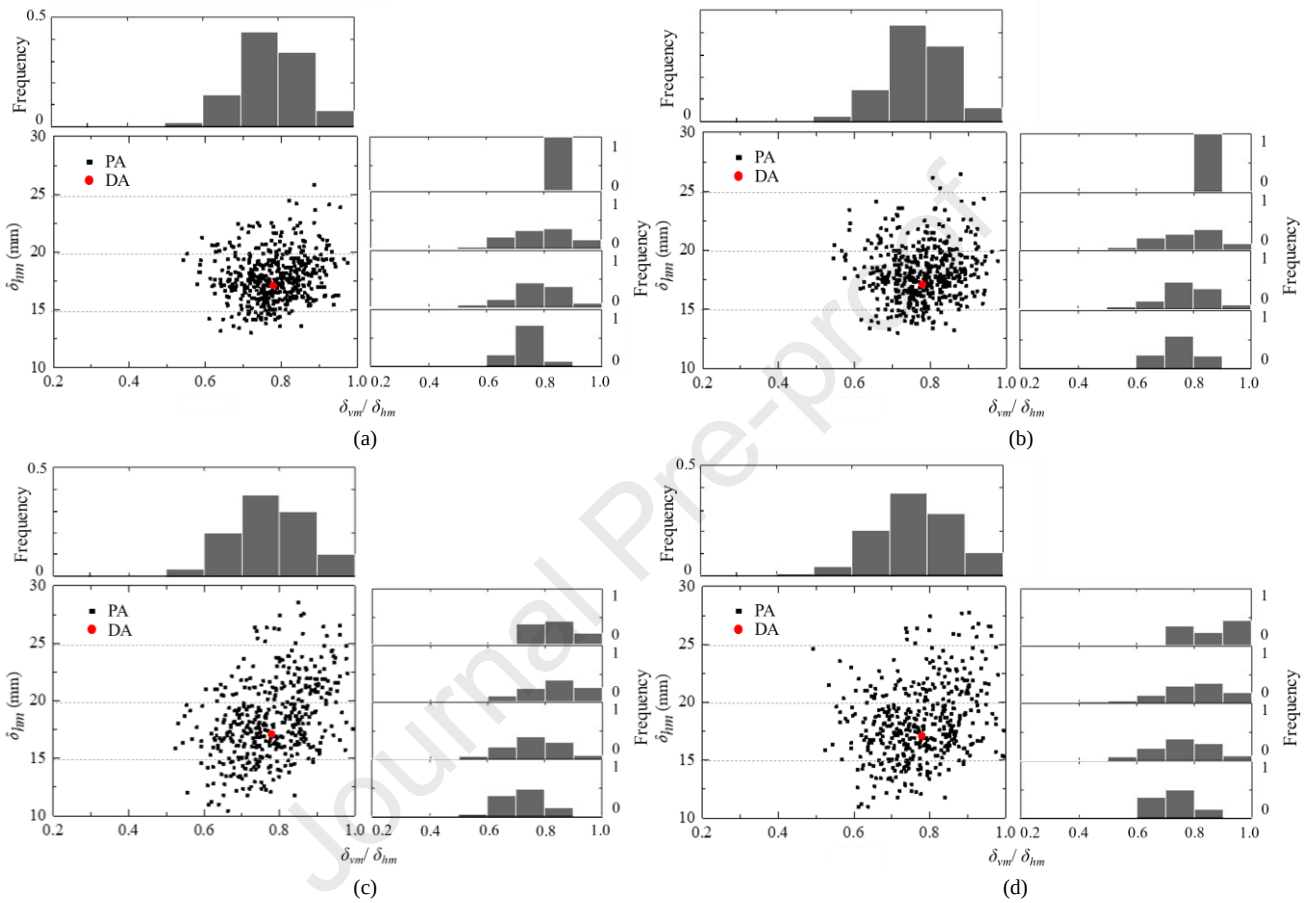

Fig. 21. Relationship between the maximum wall deflection and maximum ground surface settlement under different cases: (a) Case A, (b) Case B, (c) Case C, and (d) Case D.

5.3. Probabilistic serviceability assessment

It should be noted that the allowable thresholds in one probabilistic analysis depend on several factors, such as the soil types, supporting system and the construction safety level requirement (Zhang et al., 2015b). This section assesses the probability of serviceability limit state failure considering different limiting values. The failure mode associated with the wall deflection instead of the ground surface settlement is considered by the fact that the wall deflection is relatively easier to be predicted accurately than the ground surface settlement (Kung et al., 2007c) and is commonly used by engineers as an indicator to assess the potential damages caused by excavations (Tang, 2011).

Fig. 22 depicts the P_f value variation with the maximum horizontal wall deflection exceeding different limiting values (12-30 mm). With the increase of the limiting wall deflection, the failure probability is decreasing since higher thresholds are not easily exceeded. The P_f value variation is large for small *COV* value cases with a difference of 5 orders of magnitude. Besides, the friction angle *COV* increase can increase considerably the failure probability, which is followed by the effects of k_0 and E_{50}^{ref}. Taking the limiting wall deflection of 30 mm as an example, the P_f value varies from 1.3×10^{-5} to 6.9×10^{-4} in the COV_{E50ref} range of [0.15, 0.35], while the P_f can be up to 0.091 with the COV_{φ} increase. It highlights again the importance of the friction angle.

Besides, it is seen that when the limiting wall deflection is larger than about 17 mm, the P_f value is increased as the uncertainty increases. Conversely, the P_f is decreased. This is because the deterministic maximum horizontal wall deflection is 17.1 mm for the reference case and the peak value of wall deflection PDF corresponds to about 17 mm as shown in Fig. 8. Therefore, when the limiting value is smaller than 17 mm, the probability of exceeding the limiting value decreases with the increase in *COV* value due to the wide distributions of maximum horizontal wall deflection, and subsequently induces a smaller failure probability.

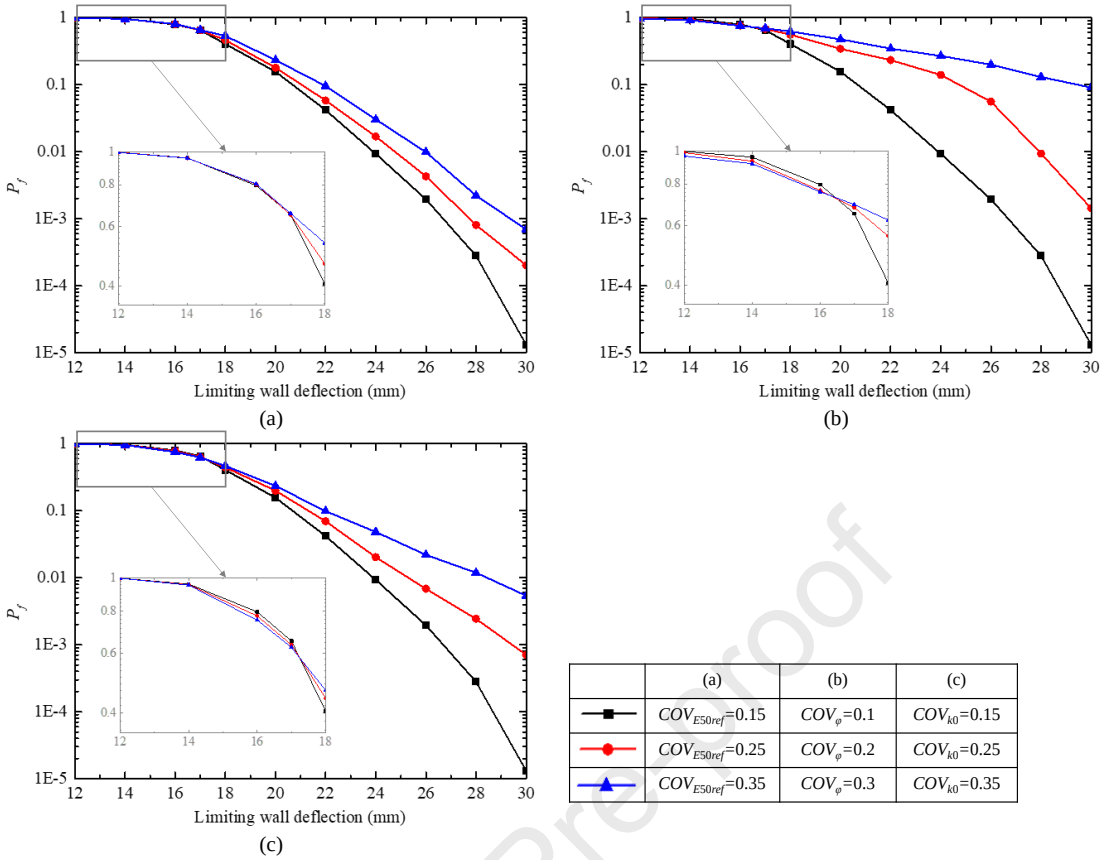

Fig. 22. Effect of parameter uncertainties on the probability of exceeding specified limiting wall deflection: (a) E_{50}^{ref}, (b) φ, and (c) k_0.

The sensitivity analysis is also implemented for different uncertainty levels and the corresponding total-effects Sobol indices can be found in Fig. 23. It is observed that with the *COV* increase, the corresponding sensitivity indices also increase. For example, the secant stiffness of layer PC has a great influence on the wall deflections and the index can be up to 0.2 when the *COV* value is equal to 0.35. Therefore, the determination of the uncertainty level should be accurately done.

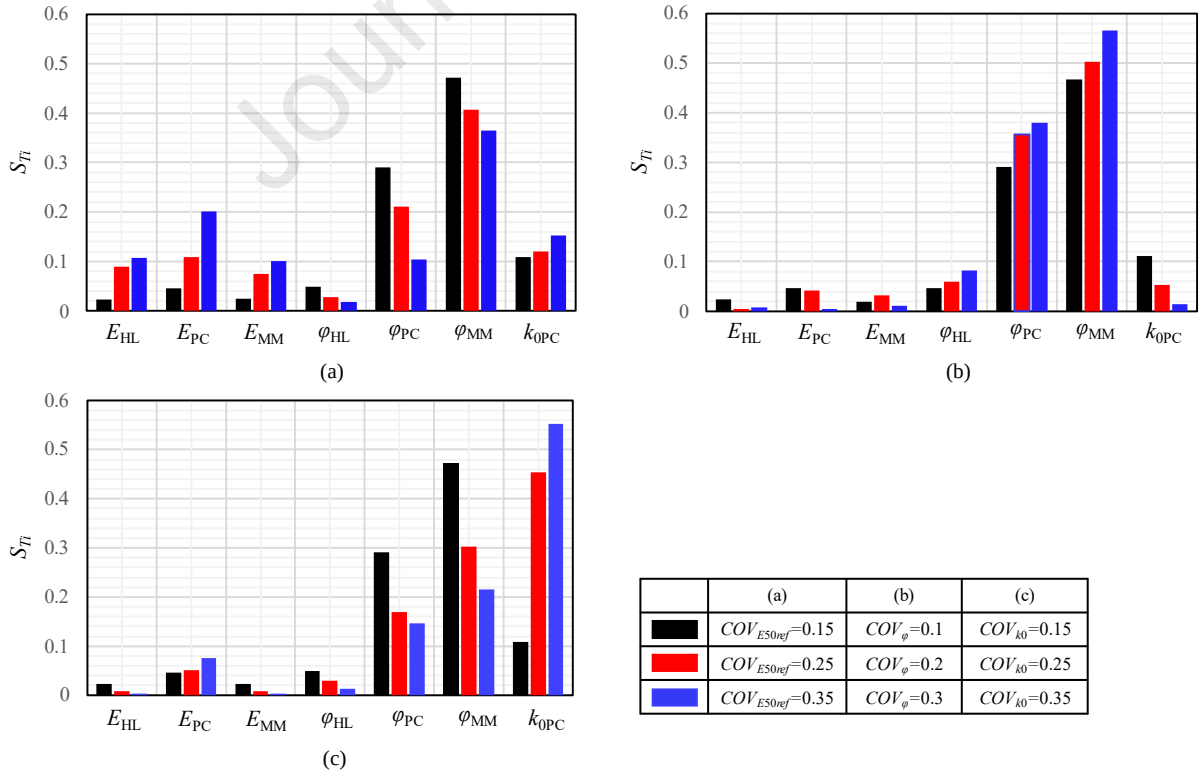

Fig. 23. Effect of parameter uncertainties on the sensitivity indices: (a) E_{50}^{ref}, (b) φ, and (c) k_0.

This section indicates that the choices of the limiting wall deflection and parameters uncertainty level play a significant role in the failure probability

calculation. Some references for the determination of the limiting wall deflection considering the related parameter uncertainties and the target serviceability failure probability are provided.

5.4. Soil-wall interaction effects

Fig. 10 shows that the plastic points are mainly distributed on the soil-wall interface, which means that the interface plays an important role in the excavation deformation. The above discussions consider the interface coefficient r_i equal to 1, while retaining wall installation or excavation construction may influence the interface strength and the horizontal wall deflection may be further affected. Therefore, the soil-wall interface strength effects on the serviceability failure probability are necessary to be explored.

The soil-wall interface strength is linked to the strength properties of the adjacent soil layer and is often reduced due to the disturbance caused by the wall construction. A range of [0.5, 1] is considered in this real case study, which is suggested by Canadian Geotechnical Society (2006), Taylor and Wang (2013) and Goh (2017) and the results are presented in Fig. 24. It can be found that with the r_i increase, the failure probability is decreasing and the P_f varies considerably for cases with small *COV* values. For example, the P_f decreases respectively about 99.9% and 68.2% for cases of COV_φ = 0.1 and COV_φ = 0.3. Besides, the parameters uncertainty level determination is more significant with the increase in soil-wall interface coefficient.

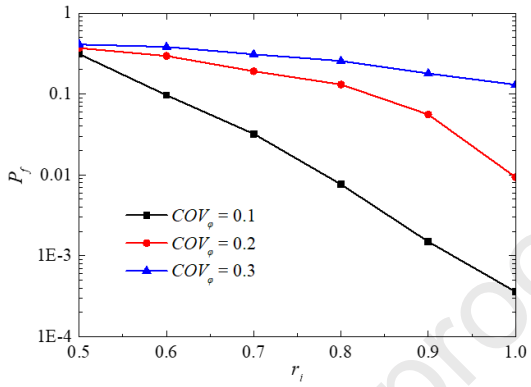

Fig. 24. Effect of the soil-wall interface on failure probability.

6. Conclusions

This paper investigates the deterministic and probabilistic stability of deep excavations based on a real case: the FIVC excavation. The FEM is adopted to predict the wall horizontal deflection and ground surface settlement. An efficient stochastic FEM based on the MSFEM is developed for the probability assessment of the serviceability limit state failure. The deterministic and probabilistic comparisons validate the FEM simulation accuracy and the proposed MSFEM. Several discussions are then conducted and the main conclusions of this paper can be summarized as follows:

(1) The horizontal wall deflections and ground surface settlements of the FIVC excavation are smaller than the former studies since (i) the FIVC station is located in a site with a considerable thickness of hard layers (HL, MM and CK); (ii) the diaphragm wall is embedded into layers MM and CK; and (iii) a multi-strutted support system is implemented. All of them can guarantee small wall deflections and ground surface settlements, which indicates that the FIVC excavation is a successful case study.

(2) The distributions of the wall deflection and ground surface settlement are wider as the *COV* value increases. The corresponding ranges for locations where the maximum wall deflection (δ_{hm}) and ground surface settlement (δ_{vm}) occur are also increased. The δ_{hm} mainly occurs from 24 m to 26 m below the ground surface, and δ_{vm} is mainly distributed in the range of [10 m, 12 m] behind the retaining wall for the FIVC excavation.

(3) The maximum ground surface settlement is linearly distributed with the maximum horizontal wall deflection and the δ_{vm}/δ_{hm} ratio is generally in the range of [0.5, 1]. It is more rational to use a larger δ_{vm}/δ_{hm} ratio to determine the δ_{vm} value for cases with larger δ_{hm}.

(4) The friction angle at the excavation bottom layer (MM) contributes the most to the model response. Parameters related to layer PC are also important by the fact that the maximum wall deflection is more likely to occur in layer PC and the corresponding parameters are sensitive to the wall deflection variations. The parameter uncertainty level also influences the sensitivity indices. It should then be determined carefully.

(5) The probability of the serviceability failure depends on the limiting wall deflection and parameters uncertainty level. The failure probability P_f increases with the *COV* value when the limiting wall deflection is larger than the deterministic wall deflection. The P_f decreases as the *COV* increases when the limiting wall deflection becomes smaller than the deterministic one. Some references for the limiting wall deflection determination are also provided.

(6) Soil-wall interface influences greatly the excavation stability, particularly for cases with small *COV* values.

This study analyzed great-depth excavations in deterministic and probabilistic frameworks. It is expected to provide useful insights and suggestions for cases with similar conditions at least in a preliminary stage. Besides, it is noted that a random variable approach is used for the parameters modeling without consideration of the soil spatial variability. Therefore, the random field theory, which can account for the spatial variability, is more realistic and will be discussed in future work (Han et al., 2023).

Declaration of competing interest

The authors declare that they have no known competing financial interests or personal relationships that could have appeared to influence the work reported in this paper.

Acknowledgments

The authors thank gratefully the China Scholarship Council for providing a PhD Scholarship (CSC No. 201906690049). The financial support is greatly appreciated.

References

Baroth, J., Malecot, Y., 2010. Probabilistic analysis of the inverse analysis of an excavation problem. Comput. Geotech. 37 (1), 391-398.

Bungenstab, F.C., Bicalho, K.V., 2016. Settlement predictions of footings on sands using probabilistic analysis. J. Rock Mech. Geotech. Eng. 8 (2), 198-203.

Canadian Geotechnical Society, 2006. Canadian foundation engineering manual. Canadian Geotechnical Society.
Clough, G.W., O'Rourke, T.D., 1990. Construction induced movements of in-situ wall, design and performance of earth retaining structures. In: ASCE, pp. 439-470.
Goh, A., 2017. Deterministic and reliability assessment of basal heave stability for braced excavations with jet grout base slab. Eng. Geol. 218, 63-69.
Guo, X., Dias, D., 2020. Kriging based reliability and sensitivity analysis-Application to the stability of an earth dam. Comput. Geotech. 120, 103411.
Guo, X., Dias, D., Carvajal, C., Peyras, L., Breul, P., 2018. Reliability analysis of embankment dam sliding stability using the sparse polynomial chaos expansion. Eng. Struct. 174, 295-307.
Guo, X., Du, D., Dias, D., 2019. Reliability analysis of tunnel lining considering soil spatial variability. Eng. Struct. 196, 109332.
Hamrouni, A., Sbartai, B., Dias, D., 2018. Probabilistic analysis of ultimate seismic bearing capacity of strip foundations. J. Rock Mech. Geotech. Eng. 10 (4), 717-724.
Han, G., Zhang, C., Singh, H.K., Liu, R., Chen, G., Huang, S., Zhou, H., Zhang, Y.T., 2023. Characterizing large-scale weak interlayer shear zones using conditional random field theory. J. Rock Mech. Geotech. Eng. 15 (10), 2611-2625.
Hong, Y., Ng, C.W.W., Liu, G.B., Liu, T., 2015. Three-dimensional deformation behaviour of a multi-propped excavation at a "greenfield" site at Shanghai soft clay. Tunn. Undergr. Space Technol. 45, 249-259.
Kung, G.T., Juang, C.H., Hsiao, E.C., Hashash, Y.M., 2007a. Simplified model for wall deflection and ground-surface settlement caused by braced excavation in clays simplified model for wall deflection and ground-surface settlement caused by braced excavation in clays. J. Geotech. Geoenvironmental Eng. 133 (6), 731-747
Kung, G.T.C., Juang, C.H., Hsiao, E.C., Hashash, Y.M., 2007b. Simplified model for wall deflection and ground-surface settlement caused by braced excavation in clays. J. Geotech. Geoenvironmental Eng. 133 (6), 731-747.
Kung, G.T.C., Hsiao, E.C., Juang, C.H., 2007c. Evaluation of a simplified small-strain soil model for analysis of excavation-induced movements. Can. Geotech. J. 44 (6), 726-736.
Liu, G.B., Jiang, R.J., Ng, C.W.W., Hong, Y., 2011. Deformation characteristics of a 38 m deep excavation in soft clay. Can. Geotech. J. 48 (12), 1817-1828.
Luo, Z., Atamturktur, S., Cai, Y., Juang, C.H., 2012. Simplified approach for reliability-based design against basal-heave failure in braced excavations considering spatial effect. J. Geotech. Geoenvironmental Eng. 138 (4), 441-450.
Luo, Z., Hu, B., Wang, Y., Di, H., 2018a. Effect of spatial variability of soft clays on geotechnical design of braced excavations: A case study of Formosa excavation. Comput. Geotech. 103, 242-253.
Luo, Z., Li, Y., Zhou, S., Di, H., 2018b. Effects of vertical spatial variability on supported excavations in sands considering multiple geotechnical and structural failure modes. Comput. Geotech. 95, 16-29.
Man, J., Zhang, T., Huang, H., Dias, D., 2023. Probabilistic analysis of tunnel face seismic stability in layered rock masses using polynomial Chaos Kriging metamodel. J. Rock Mech. Geotech. Eng.
Marelli, S., Sudret, B., 2014. UQLab: A framework for Uncertainty Quantification in MATLAB. Vulnerability, Uncertainty, Risk ©ASCE 2554-2563.
Mayne, P., Kulhawy, F., 1982. K0-OCR relationships in soil. ASCE GT6. 851-869.
Nejjar, K., 2019. Comportement des parois de soutènement dans un contexte exceptionnel (grande profondeur, formations déformables, environnement sensible). PhD Thesis. Grenoble Alpes University, Grenoble, France.
Nejjar, K., Dias, D., Cuira, F., Chapron, G., Lebissonnais H., 2021. Experimental study of the performance of a 32 m deep excavation in the suburbs of Paris. Géotechnique. 73 (6), 469-479..
Ng, C.W.W., Hong, Y., Liu, G.B., Liu, T., 2012. Ground deformations and soil-structure interaction of a multi-propped excavation in Shanghai soft clays. Geotechnique. 62 (10), 907-921.
Nguyen, T.S., Likitlersuang, S., 2021. Influence of the spatial variability of soil shear strength on deep excavation: A Case Study of a Bangkok Underground MRT Station. Int. J. Geomech. 21 (2), 04020248
O'Rourke, T.D., 1993. Base stability and ground movement prediction for excavations in soft clay. Thomas Telford, London.
Pan, Q., Dias, D., 2017. Probabilistic evaluation of tunnel face stability in spatially random soils using sparse polynomial chaos expansion with global sensitivity analysis. Acta Geotech. 12, 1415-1429.
Pan, Q., Qu, X., Liu, L., Dias, D., 2020. A sequential sparse polynomial chaos expansion using Bayesian regression for geotechnical reliability estimations. Int. J. Numer. Anal. Methods Geomech. 44 (6), 874-889.
Peck, R.B., 1969. Deep excavations and tunneling in soft ground. In Proceedings of the 7th international conference on soil mechanics and foundation engineering (ICSMFE). Mexico, pp. 225-290.
Philipponnat, G., Hubert, B., 2016. Fondations et ouvrages en terre. Eyrolles.
Phoon, K.K., Kulhawy, F.H., 1999. Characterization of geotechnical variability. Can. Geotech. J. 36 (4), 612-624.
Rouainia, M., Elia, G., Panayides, S., Scott, P., 2017. Nonlinear finite-element prediction of the performance of a deep excavation in Boston blue clay. J. Geotech. Geoenvironmental Eng. 143 (5), 04017005.
Schöbi, R., Sudret, B., Marelli, S., 2017. Rare Event Estimation Using Polynomial-Chaos Kriging. ASCE ASME J. Risk Uncertain. Eng. 3 (2), D4016002.
Sert, S., Luo, Z., Xiao, J., Gong, W., Juang, C.H., 2016. Probabilistic analysis of responses of cantilever wall-supported excavations in sands considering vertical spatial variability. Comput. Geotech. 75, 182-191.
Tan, Y., Wei, B., 2012. Observed behaviors of a long and deep excavation constructed by cut-and-cover technique in Shanghai soft clay. J. Geotech. Geoenvironmental Eng. 138 (1), 69-88.
Tang, Y., 2011. Probability-based method using RFEM for predicting wall deflection caused by excavation. J. Zhejiang Univ.: Sci. A. 12, 737-46.
Taylor, P., Wang, Y., 2013. MCS-based probabilistic design of embedded sheet pile walls. Georisk. 7, 151-162.
Tran, N.T., Do, D.P., Hoxha, D., Vu, M.N., Armand, G., 2021. Kriging-based reliability analysis of the long-term stability of a deep drift constructed in the Callovo-Oxfordian claystone. J. Rock Mech. Geotech. Eng. 13 (5), 1033-1046.
Wang, Z.W., Ng, C.W.W., Liu, G.B., 2005. Characteristics of wall deflections and ground surface settlements in Shanghai. Can. Geotech. J. 42 (5), 1243-1254.
Xue, Y., Miao, F., Wu, Y., Dias, D., Li, L., 2023. Combing soil spatial variation and weakening of the groundwater fluctuation zone for the probabilistic stability analysis of a riverside landslide in the Three Gorges Reservoir area. Landslides. 1-17.
Yang, Z., Chen, Y., Azzam, R., Yan, C., 2022. Performance of a top-down excavation in shanghai: case study and numerical exploration. Eur. J. Environ. Civ. Eng. 26 (5), 7932-7957.
Zhang, R., Wu, C., Goh, A., Thomas, B., Zhang, W., 2021. Estimation of diaphragm wall deflections for deep braced excavation in anisotropic clays using ensemble learning. Geosci. Front. 12 (1), 365-373.
Zhang, R., Zhang, W., Goh, A., Hou, Z., Wang, W., 2018a. A simple model for ground surface settlement induced by braced excavation subjected to a significant groundwater drawdown. Geomech. Eng. 16, 635-642.
Zhang, T., An, L., Dias, D., Baroth, J., Li, C., 2023. Sample-wised probabilistic stability analysis of circular shafts using the Atom Search Optimization-based Artificial Neural Network. Eng. Struct. 294, 116718.
Zhang, T., Baroth, J., Dias, D., 2022. Deterministic and probabilistic basal heave stability analysis of circular shafts against hydraulic uplift. Comput. Geotech. 150, 104922.
Zhang, T., Baroth, J., Dias, D., 2021. Probabilistic basal heave stability analyses of supported circular shafts in non-homogeneous clayey soils. Comput. Geotech. 140, 104457.

Zhang, W., Goh, A., Xuan, F., 2015a. A simple prediction model for wall deflection caused by braced excavation in clays. Comput. Geotech. 63, 67-72.
Zhang, W., Goh, A., Zhang, Y., 2015b. Probabilistic Assessment of serviceability limit state of diaphragm walls for braced excavation in clays. ASCE ASME J. Risk Uncertain. Eng. 1 (3), 06015001.
Zhang, W., Wang, W., Zhou, D., Zhang, R., Goh, A., Hou, Z., 2018b. Influence of groundwater drawdown on excavation responses–A case history in Bukit Timah granitic residual soils. J. Rock Mech. Geotech. Eng. 10 (5), 856-864.
Zhang, W., Zhang, R., Wang, W., Zhang, F., Teck, A., Goh, C., 2019. A multivariate adaptive regression splines model for determining horizontal wall deflection envelope for braced excavations in clays. Tunn. Undergr. Space Technol. 84, 461-471.
Zhao, J., Ritter, S., DeJong, M.J., 2022. Early-stage assessment of structural damage caused by braced excavations: Uncertainty quantification and a probabilistic analysis approach. Tunn. Undergr. Space Technol. 125, 104499.
Zheng, G., Yang, X., Zhou, H., Du, Y., Sun, J., Yu, X., 2018. A simplified prediction method for evaluating tunnel displacement induced by laterally adjacent excavations. Comput. Geotech. 95, 119-128.

Dr. Tingting Zhang obtained her MSc degree from Hefei University of Technology (China) in 2019, and her PhD in Geotechnical Engineering from Université Grenoble Alpes (France) in 2023, respectively. She is working as a postdoctoral researcher in Geotechnical Engineering at Université de Lorraine (France). Her main research topic is the probabilistic analysis of geotechnical structures, such as excavations, tunnels, slopes, shafts and dams. In deterministic frameworks, the limit analysis methods and numerical simulations are mainly used. In probabilistic framework, the surrogate models, which can be constructed by the Kriging, Polynomial Chaos Expansion, Polynomial Chaos Kriging, and machine learning methods, etc., are introduced to improve the computational efficiency. In addition, a sensitivity analysis based on the global sensitivity method was conducted to explore the effect of parameters. She also conducted research on back analysis.

Declaration of interests

☒ The authors declare that they have no known competing financial interests or personal relationships that could have appeared to influence the work reported in this paper.

☐The authors declare the following financial interests/personal relationships which may be considered as potential competing interests: